Physics of Plasmas

Magnetospheric chorus wave simulation with the TRISTAN-MP PIC code

Cite as: Phys. Plasmas **26**, 072901 (2019); https://doi.org/10.1063/1.5096537
Submitted: 18 March 2019 . Accepted: 11 June 2019 . Published Online: 11 July 2019

I. V. Kuzichev, A. R. Soto-Chavez, J. Park, A. Gerrard, and A. Spitkovsky

Physics of Plasmas ARTICLE scitation.org/journal/php

Magnetospheric chorus wave simulation with the TRISTAN-MP PIC code

Cite as: Phys. Plasmas **26**, 072901 (2019); doi: 10.1063/1.5096537
Submitted: 18 March 2019 · Accepted: 11 June 2019 ·
Published Online: 11 July 2019

I. V. Kuzichev,[1,a)] A. R. Soto-Chavez,[1] J. Park,[2] A. Gerrard,[1] and A. Spitkovsky[3]

AFFILIATIONS

[1]Center for Solar-Terrestrial Physics, New Jersey Institute of Technology, Newark, New Jersey 07102, USA
[2]Lawrence Berkeley National Lab, Berkeley, California 94720, USA
[3]Department of Astrophysical Sciences, Peyton Hall, Princeton University, Princeton, New Jersey 08544, USA

[a)]**Also at:** Space Research Institute of RAS, Moscow 117997, Russia.

ABSTRACT

We present the results of particle-in-cell simulations of the whistler anisotropy instability that results in magnetospheric chorus wave excitation. The simulations were carried out using, for the first time for this problem, the 2D TRISTAN-massively parallelized code, widely used before in the modeling of astrophysical shocks. The code has been modified to allow for two populations of electrons: cold electrons (which maintain the wave propagation) and hot electrons (which provide the wave growth). For the hot electrons, the anisotropic form of the relativistic Maxwell–Jüttner distribution is implemented. We adopt the standard approximation of a parabolic magnetic field to simulate the Earth's magnetic field close to the equator. Simulations with different background magnetic field inhomogeneity strengths demonstrate that higher inhomogeneity yields lower frequency chirping rates and, eventually, it suppresses chorus generation. The results are in agreement with other numerical simulations and the theoretical predictions for the frequency chirping rates.

I. INTRODUCTION

Magnetospheric chorus waves are one of the most important and interesting wave phenomena in the Earth's radiation belts. They belong to the whistler mode and have frequencies from hundreds of hertz to several kilohertz. Chorus waves are often observed by satellites as discrete series of wave packets with varying frequency, mostly rising,[1] but falling-tone chorus are also found.[2,3] Generally, chorus waves are separated into two bands: lower-band chorus waves with frequencies $\omega_{LH} \ll \omega < 0.5\ \omega_{ce}$, where ω_{LH} is the lower hybrid frequency and ω_{ce} stands for electron cyclotron frequency, and upperband chorus waves $0.5\ \omega_{ce} < \omega < \omega_{ce}$.[4] There usually exists a gap in the wave spectrum at $0.5\ \omega_{ce}$, but there are also some observations of chorus wave spectra without it.[5]

Chorus waves play a significant role in the radiation belt dynamics: being one of the most intense wave phenomena, they lead to particle acceleration[6] and precipitation[7,8] via resonant wave-particle interactions.[9,10] Despite being investigated for the last 30 years, generation of rising and falling tone chorus waves is still not fully understood. For the rising-tone chorus waves, different theories were proposed. A theory developed by Omura *et al.*[11] shows that the chorus frequency chirping contributes to the total inhomogeneity parameter of the dynamical system in such a way that it maximizes nonlinear current and, consequently, the growth rate of the wave. The nonlinear current is associated with the formation of an electromagnetic phase space electron hole.[11,12] This theory was developed for chorus waves which propagate parallel to background magnetic field. These waves resonantly interact with electrons via first cyclotron resonance. Satellite observations[13] show that this assumption is quite reasonable because chorus wave normal angles in the equatorial regions are mostly small, that is, the waves propagate along the field lines. Nevertheless, a significant fraction of oblique chorus waves (with wave normal angles $\gtrsim 50°$) is also observed, specifically for upperband chorus waves.[14] The small obliquity of chorus wave propagation has been taken into account theoretically by Omura *et al.*,[15] and it has been shown to be a possible mechanism for the formation of the gap between lower- and upper-band chorus waves.[16] The obliquity of the wave gives rise to an infinite set of cyclotron resonances at harmonics of electron cyclotron frequency, and to Landau resonance, which could lead to strong wave damping.[17] This damping might account for the above-mentioned gap (even in the case of small wave normal angles), but it might also lead to decay of electromagnetic hole associated with the formation of nonlinear current and, eventually, with the chorus wave growth and frequency chirping.[16] Huang *et al.*[18] attempted to explain the gap for the parallel chorus waves by analyzing a specific type of electron

distribution function which gives two maxima for the linear growth rate, one in the lower band frequency range and another in the upper band. The authors generated distinct upperband and lowerband chorus waves with one dimensional (1D) particle in cell (PIC) code, but the gap between the bands was defined by the initial distribution function, and was not necessarily at 0.5 ω_{ce}. Another interesting property of the chorus wave generation that might contribute to the gap formation was considered by Hosseini *et al.*[19] The authors explain that the upperband chorus waves are sometimes triggered by the lightning-induced whistlers. Their analysis suggests that there is a trade-off between the linear growth rate and the lowest critical wave amplitude required for the nonlinear effects to be present. This leads to the preferential triggering of the upperband chorus waves, while the lowerband chorus waves are generated spontaneously via the whistler anisotropy instability.

Another theory, the backward wave oscillator (BWO) model, was developed by Trakhtengerts.[20] This model suggests that chorus waves are excited due to a steplike deformation in the particle parallel momentum distribution function. The height of the step on the velocity distribution function is a free parameter of the model.[21]

Falling-tone chorus waves show slightly different properties from the rising-tone waves, such as large oblique propagation angles and different peak amplitudes; therefore, different mechanisms have been proposed. For example, Soto-Chavez *et al.*[17] introduced the idea that falling-tone chorus may be generated by simultaneously exciting two competing resonances (Landau and cyclotron), whereby a marginal stable falling-tone mode is formed. The marginally unstable mode will perturb the electron distribution function such that a clump-hole pair develops, further amplifying the wave. However, the dominant structure is the clump in the distribution function which generates the falling tone. In the framework of the Omura *et al.* theory,[16] falling-tone chorus waves might be explained as the result of formation of a hill on the distribution function instead of the hole. While the hole leads to rising-tone emission, the hill can produce falling-tone elements.[16] This idea is supported by a numerical simulation with a hybrid Vlasov code,[22] but this numerical model has certain limitations and assumptions. For example, it requires a triggering wave which leads to the chorus wave excitation in the upstream region with respect to geomagnetic equator, and also requires a reduction of the downstream region to suppress dominant rising-tone wave generation. The BWO model also reproduces falling-tone elements in simulations, e.g., Demekhov[23] has shown that falling-tone chorus waves can be generated near the boundaries of the BWO generation region if these boundaries are close enough to magnetic mirror points for the particles.

The common feature of most of the chorus theoretical models is that they are nonlinear. Nonlinearity of the corresponding processes significantly reduces the opportunities to study them analytically. Hence, numerical modeling is required. Vlasov codes, which yield low statistical noise,[24] are very expensive in terms of computational resources and, therefore, are rarely used for the problem under consideration. Nevertheless, some simplified versions of this approach, with Eulerian numerical schemes[25,26] and with finite difference schemes,[27] proved to be very useful for chorus wave modeling. The most commonly used approach is particle in cell (PIC) modeling, which provides the possibility to account for self-consistent kinetic dynamics.[28] For example, in Refs. 12 and 29–32, the problem is studied with one dimensional (1D) PIC codes, some hybrid (that is, treating cold electron population as fluid and hot electrons, participating in resonant interactions, as particles), and some fully kinetic. The majority of PIC simulations tend to use rather large temperature anisotropies which exceed the anisotropies typically observed in the chorus generation region[33] due to the limitations of numerical resources. On the other hand, numerical studies of the BWO model do not require large temperature anisotropy because the model assumes sharp gradients in the parallel velocity space.[23] This modeling shows results consistent with some observations (see, e.g., Refs. 21, 34, and 35). However, to the best of our knowledge, no fully kinetic simulations have been carried out in relation to the BWO model. A review of numerical approaches to the nonlinear cyclotron resonance can be found in Ref. 36.

This paper presents new results of numerical simulations of the magnetospheric chorus wave generation with a full 2D particle-in-cell (PIC) code. We have modified the TRISTAN-massively parallelized (MP) code[37–39] in such a way that it would be applicable to this problem, and we were able to successfully generate chorus waves with this code. In particular, we developed a numerical scheme to inject two electron populations in the TRISTAN-MP code. We implemented the correct anisotropic relativistic distribution, according to which the hot electrons are sampled in the code. We also implemented particle reflection at the boundary of the simulation box to simulate magnetically mirroring particles and absorption boundary conditions for the waves to simulate the effect of wave propagation away from the box. One of the purposes of the present study is to investigate chorus wave generation in quasiparallel regime, but without one-dimensional approximation that has been used in 1D PIC codes.

The paper is structured as follows. Section II contains detailed information on the simulation model we use. In Sec. III, we discuss the results of a linear theory of the whistler instability for the particle distribution, specified in Sec. II. Section IV contains the results of the numerical modeling, which are summarized in Sec. V.

II. SIMULATION SETUP

We consider two electron populations: cold electrons, which maintain the wave propagation, and hot electrons with anisotropic biMaxwellian distribution. The hot population takes part in resonant wave-particle interaction, providing energy exchange between particles and waves. We consider relativistic hot electrons. Unlike in some previous studies,[32] where direct extrapolation of the nonrelativistic biMaxwellian to the relativistic energies was used, we implement the distribution with the correct relativistic limit.

In the relativistic case, the correct isotropic Maxwell distribution is the Maxwell–Jüttner distribution, which can be written as

$$F(\vec{p}) = Ne^{-\frac{mc^2}{T}\gamma(\vec{p})}, \tag{1}$$

where N is a normalization constant, and γ is the Lorentzfactor

$$\gamma(\vec{p}) = \sqrt{1+\frac{p^2}{(mc)^2}}. \tag{2}$$

(Further, we will use the units $m = c = 1$.) One can see that, unlike the nonrelativistic case, the distribution cannot be represented as a product of one-dimensional distributions. This makes the generalization of Eq. (1) to an anisotropic case less straightforward than the nonrelativistic Maxwell distribution.[40] We will use the following form of the distribution:

$$F(\vec{p}) = Ne^{-\frac{1}{T}\sqrt{1+\frac{p_\parallel^2}{\sin^2\delta}+\frac{p_\perp^2}{\cos^2\delta}}}, \tag{3}$$

where δ is a parameter governing the anisotropy. This distribution has the correct isotropic limit, corresponding to Maxwell–Jüttner distribution, and the correct nonrelativistic limit, where it corresponds to the ordinary nonrelativistic biMaxwellian distribution.

Note that the distribution functions of the type

$$F(\vec{p}) = Ne^{-\frac{p_\parallel^2}{2T_\parallel}-\frac{p_\perp^2}{2T_\perp}} \tag{4}$$

used in some previous studies of the chorus wave generation[31,32] are not relativistic biMaxwellian distributions in the above sense. That is, they do not become the Maxwell–Jüttner (1) distribution in the limit of zero anisotropy. In particular, for ultrarelativistic particles $p \gg 1$, (4) behaves as $\exp\left(-\frac{p^2}{T}\right)$, while the Maxwell–Jüttner distribution (1) behaves as $\exp\left(-\frac{p}{T}\right)$.

In our case, however, the biMaxwellian (3) defines particle momentum distribution at the equator only because of the background magnetic field inhomogeneity. So, in order to set the initial particle distribution in the whole region of space, we use the adiabatic approximation. That is, we assume that in the absence of the waves, the particle energy and the particle first adiabatic invariant (magnetic moment) are conserved. Hence, we can restore the particle phase space density at any point, using the Liouville's theorem

$$F(\vec{p},\vec{r}) = F_{eq}\left(\vec{p}_{eq},\vec{r}_{eq}\right). \tag{5}$$

Here, equatorial variables are related to variables in a given position through the conservation laws

$$\begin{aligned} p_\parallel^2 + p_\perp^2 &= p_{eq\parallel}^2 + p_{eq\perp}^2, \\ \frac{p_\perp^2}{B(\vec{r})} &= \frac{p_{eq\perp}^2}{B_{eq}}. \end{aligned} \tag{6}$$

Solving these equations and taking into account expression (3) for the distribution at the equator, one gets for the distribution function at a given point

$$\begin{aligned} F(\vec{p},\vec{r}) &= Ne^{-\frac{1}{T}\sqrt{1+\frac{p_\parallel^2}{\sin^2\delta}+\frac{p_\perp^2}{\cos^2\delta}h(\vec{r})}}, \\ h(\vec{r}) &= 1 + A\left(1-\frac{B_{eq}}{B(\vec{r})}\right), \end{aligned} \tag{7}$$

where $A = \cos^2\delta/\sin^2\delta - 1$ is the anisotropy parameter.

We consider a 2D system with parabolic background magnetic field

$$\begin{aligned} B_x &= B_0(1+\alpha x^2), \\ B_y &= -2B_0\alpha x(y-y_0). \end{aligned} \tag{8}$$

Here the x coordinate represents the length along the field line, $x = 0$ corresponds to the magnetic equator, and the inhomogeneity parameter α governs the variation of the magnetic field along the field line. The transverse component of the magnetic field, B_y, is added in order to satisfy Maxwell's equation $\mathrm{div}\vec{B} = 0$. The distribution of the magnetic field is shown in Fig. 1.

For the simulations presented in this study, we use the following dimensions of the simulation box: $L_x \approx 432[\frac{c}{\omega_{ce}}]$ and $L_y \approx 4[\frac{c}{\omega_{ce}}]$. All quantities depend (vary) only on these coordinates and time. Particles have 3-dimensional momentum and coordinate. We use two electron populations with two different temperatures, $T_{hot} \approx 100$ keV and $T_{cold} = 0$. We should mention that here we refer to T_{hot} as to the parameter $T = T_\perp + T_\parallel$ in Eq. (7). The actual temperature is $(T_\parallel + 2T_\perp)/3$. The anisotropy angle, defined in Eq. (3), is $\delta = 0.4$, yielding for the hot particles $T_\perp \approx 85$ keV and $T_\parallel \approx 15$ keV. This gives an anisotropy parameter $A = T_\perp/T_\parallel - 1 \approx 4.6$. Such a value of A is rather large as compared to values observed in the outer radiation belt, but reducing the anisotropy significantly lowers the linear wave growth rate, which makes numerical simulation in 2D (and even in 1D[32]) too consuming with respect to computational resources. The hot-to-cold electron density ratio is taken to be $n_h/n_c = 0.01$. Note that this ratio decreases further away from the equator since the particles are distributed adiabatically, which for hot anisotropic particles means an inhomogeneous distribution. Meanwhile, the cold particles are distributed homogeneously. The ratio of plasma and cyclotron frequency is $\sigma = \frac{\omega_{pe}}{\omega_{ce}} = 5$. We consider different inhomogeneity parameters $\alpha \in (0.125, 1.0) \times 10^{-5}\,[\frac{\omega_{ce}^2}{c^2}]$. The intermediate value, $\alpha = 0.5 \times 10^{-5}\,[\frac{\omega_{ce}^2}{c^2}]$, of the inhomogeneity parameter for a given length of the box gives about a 10% increase in magnetic field at the boundaries with respect to the equator, which corresponds to $\sim 5^\circ$ of magnetic latitudes for the Earth's dipole magnetic field. The full list of the simulation parameters is shown in Table I. In this Table, $\Delta_{x,y}$ stands for spatial grid size in the x and y dimension, respectively, Δ_t is time step, and N_{ppc} defines the number of particles in one spatial cell. This number includes ions, cold electrons, and hot electrons. In total, the dynamics of approximately 387 million particles was simulated. The number of particles used in the present simulation is more than the number of particles used in typical one dimensional PIC simulations of chorus waves (see, e.g., Refs. 31, 32, and 41).

An example of the initial hot electron distribution sampled from Eq. (7) with inhomogeneity $\alpha = 0.5 \times 10^{-5}\,[\frac{\omega_{ce}^2}{c^2}]$ is presented in Fig. 2. To restore the distribution function from particle data, which contains particle phase space coordinates, we used area-weighted interpolation of the particle density to grid in the momentum and spatial coordinate domain. The left column of Fig. 2 shows the hot electron distribution at the equator, while the distribution far from the equator is shown in the right column. The upper panels show the momentum distribution $F(p_\parallel, p_\perp)$. The distributions presented in this figure are normalized on $\int F_e(p_\parallel, p_\perp, x = 0)\, dp_\parallel dp_\perp$. We should note that the distribution shown includes the Jacobian of transformation to polar coordinates in transverse momentum space $(p_y, p_z) \to (p_\perp, \phi)$. The relation between this distribution and the actual phase space density of the particles is

$$F(p_\parallel, p_\perp, \vec{r}) = \int F\left(p_\parallel, p_z(p_\perp,\phi), p_y(p_\perp,\phi), \vec{r}\right) p_\perp d\phi. \tag{9}$$

The 1D distributions shown in the lower panels are obtained by integrating $F(p_\parallel, p_\perp)$ over one of the momenta. Red lines correspond to the numerical particle sample, while analytical distributions obtained from Eq. (7) are presented by green lines.

III. LINEAR THEORY

The waves are generated from the statistical noise due to whistler anisotropy instability.[42] The relativistic generalization of the linear

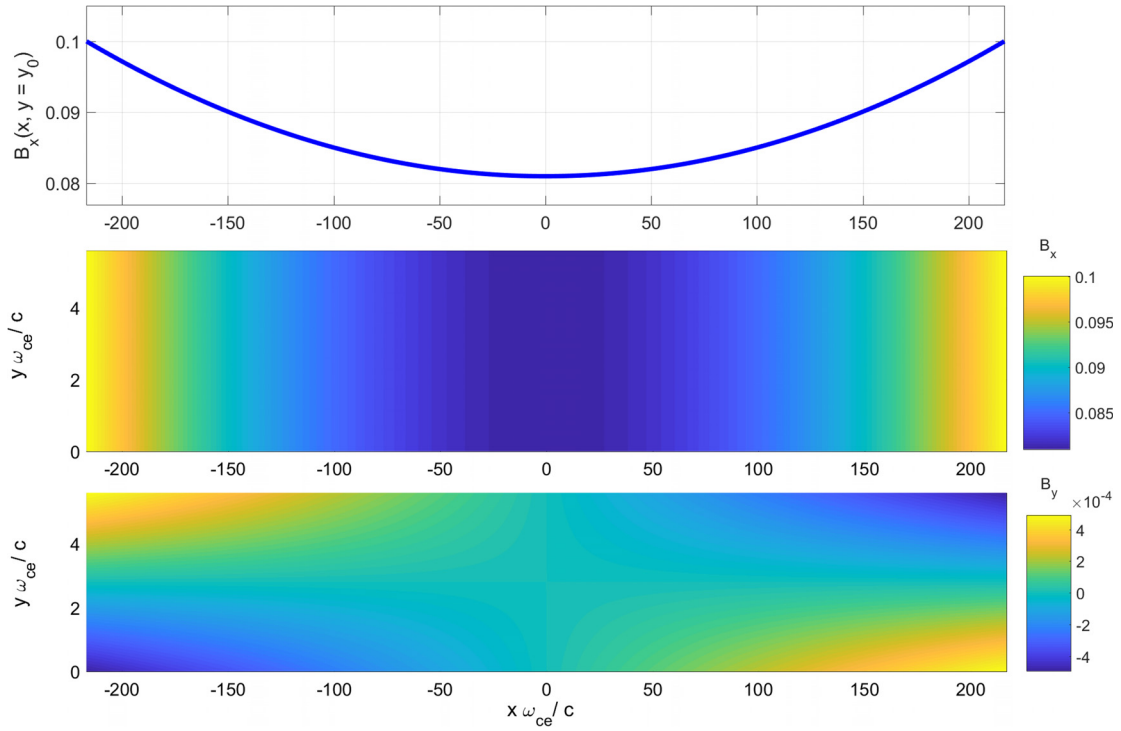

FIG. 1. Parabolic background magnetic field for inhomogeneity $\alpha = 0.5\times10^{-5}\ [\frac{\omega_{ce}^2}{c^2}]$. The upper panel shows the dominant B_x component of the field as a function of x. The middle panel shows the (x, y) distribution of this component. The lower panel shows the $B_y(x, y)$ component of the background magnetic field. The background magnetic field satisfies zero divergence condition.

theory of this instability can be found in the work of Xiao *et al.*[43] In this section, we discuss the results of the linear theory for the distribution function (7) that we have chosen for the simulations.

The frequencies of the upper and lower-band chorus waves usually belong to the range $[0.05\ \omega_{ce}, 0.9\ \omega_{ce}]$, when the electron cyclotron frequency ω_{ce} is less than electron plasma frequency ω_{pe}. In such cases, the ion contribution to the dispersion equation for the wave can be neglected because the wave frequency is much larger than the proton cyclotron frequency, $\omega \gg \omega_{cp}$. The linear dispersion relation for the waves propagating parallel to the Earth's magnetic field lines would then be

$$k^2 = \omega^2 + \frac{\omega\omega_{pe}^2}{\omega_{ce} - \omega}, \tag{10}$$

where k is the wave number, i.e., the absolute value of the wave vector.

The resonant wave-particle interaction takes place for the particles satisfying the following resonance condition:

$$p_{\parallel} = \frac{\gamma\omega - \omega_{ce}}{k}. \tag{11}$$

In contrast to the nonrelativistic case (see, e.g., the in-depth review[10]), the resonance condition does not simply define the resonant parallel momentum p_r as a function of spatial coordinates (through the spatial dependency of ω_{ce}), but it represents a relation between both particle momenta, parallel and perpendicular, through the Lorentz factor γ, and the spatial coordinate. Solving for $p_{\parallel}$, one gets from this equation the following expression for the resonant parallel momentum and resonant γ:

$$\begin{aligned} p_r &= \frac{\omega\gamma_r - \omega_{ce}}{k}, \\ \gamma_r &= \left[-\frac{\omega_{ce}}{\omega} + \sqrt{\frac{\omega_{ce}^2}{\omega^2} + \left(\frac{k^2}{\omega^2} - 1\right)\left(\frac{\omega_{ce}^2}{\omega^2} + \frac{k^2}{\omega^2}\left(p_{\perp}^2 + 1\right)\right)}\right] \Big/ \left[\frac{k^2}{\omega^2} - 1\right]. \end{aligned} \tag{12}$$

TABLE I. List of simulation parameters for all runs.

$L_x, \left[\frac{c}{\omega_{ce}}\right]$	$L_y, \left[\frac{c}{\omega_{ce}}\right]$	$\Delta_x = \Delta_y, \left[\frac{c}{\omega_{ce}}\right]$	$\Delta_t, \left[\frac{1}{\omega_{ce}}\right]$	N_{ppc}	$T_e^{(h)}$, keV	δ	$\sigma = \frac{\omega_{pe}}{\omega_{ce}}$	$\delta n = \frac{n_h}{n_c}$
432	4	0.4	0.18	4×10^4	100	0.4	5	0.01

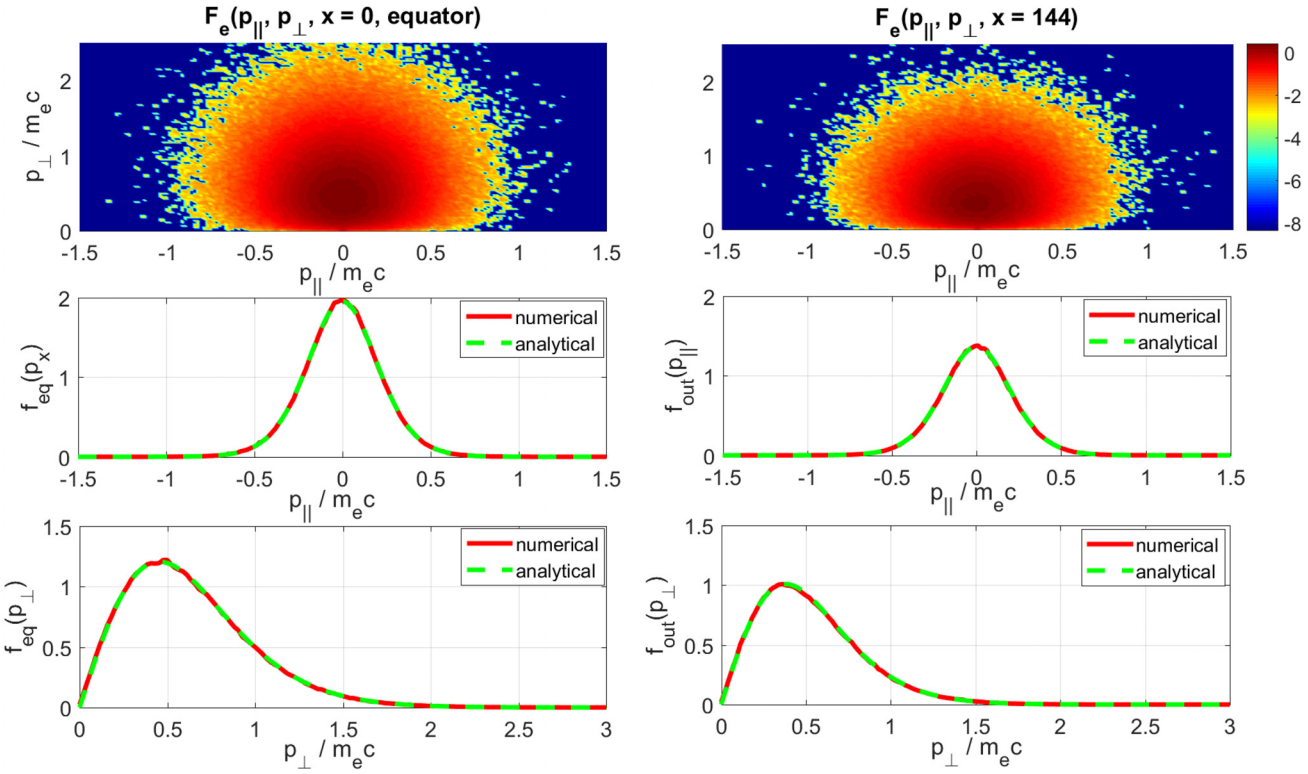

FIG. 2. Initial normalized distribution for inhomogeneity parameter $\alpha = 0.5\times10^{-5}\ [\frac{\omega_{ce}^2}{c^2}]$ in two different positions along the field line: at the equator (left panels) and away from the equator, near the boundary of the simulation box (right panel). All the distributions are normalized to the momentum integral of the distribution at the equator. The upper panels show 2D momentum distributions, and the lower panels demonstrate the distributions, integrated over one of the momenta. Green lines represent analytical distributions, while red lines correspond to the distributions recovered from numerical particle sample.

Xiao *et al.*[43] have shown the linear growth rate of the waves to be

$$\Gamma_{lin} = \frac{\pi\omega_{pe}^2\eta}{2\omega + \omega_{pe}^2\omega_{ce}/(\omega-\omega_{ce})^2}(A[F] - A_{thr}). \tag{13}$$

Here, $A[F]$ represents a measure of the anisotropy of the given distribution function F. It should be mentioned that, for the nonrelativistic biMaxwellian distribution, $A[F]$ is equal to the anisotropy parameter A defined above, right after Eq. (7). For an arbitrary distribution function

$$A[F] = \frac{\dfrac{k}{\omega-\omega_{ce}}\displaystyle\int_0^\infty \frac{dp_\perp}{\Delta}\frac{p_\perp^2}{\gamma_r}\left(p_\perp\frac{\partial F}{\partial p_\parallel} - p_\parallel\frac{\partial F}{\partial p_\perp}\right)_{p_\parallel=p_r}}{\displaystyle\int_0^\infty \frac{dp_\perp}{\Delta}p_\perp^2\left(\frac{\partial F}{\partial p_\perp}\right)_{p_\parallel=p_r}}, \tag{14}$$

where $\Delta = 1 - \omega p_r/\gamma_r k$. A_{thr} gives the anisotropy threshold

$$A_{thr} = \frac{\omega}{\omega_{ce}-\omega}. \tag{15}$$

The quantity η is related to the fraction of resonant particles

$$\eta = \pi\frac{n_h}{n_c}\frac{\omega-\omega_{ce}}{k}\int_0^\infty \frac{dp_\perp}{\Delta}p_\perp^2\left(\frac{\partial F}{\partial p_\perp}\right)_{p_\parallel=p_r}, \tag{16}$$

where n_h/n_c stands for the hot to cold electrons density ratio. As follows from Eq. (13), the sign of Γ_{lin} is defined by the balance of $A[F]$ and A_{thr} since, in our case, η is non-negative. The waves can be excited in the linear regime only in the case when $\Gamma_{lin} > 0$. Figure 3 gives an example of frequency dependency of these parameters for the distribution under consideration.

The left panel of Fig. 3 shows linear increment as a function of wave frequency for 3 different types of distribution: the relativistic biMaxwellian distribution, corresponding to the Maxwell–Jüttner distribution, Eq. (3); the distribution (4) used in previous studies;[32] and the nonrelativistic biMaxwellian with nonrelativistic form of Γ_{lin}. One can see that the difference between linear increments is rather noticeable. First of all, in spite of the fact that the resonance velocity is only slightly relativistic, the relativistic effects are important, providing a difference of about 40% in maximum increment. The reason for this is that the relativistic resonance condition involves perpendicular energy, which is higher than the parallel. Secondly, the increment for the anisotropic Maxwell–Jüttner distribution (3) is shifted toward lower frequencies with respect to the one obtained from distribution (4) for the same parameters. The right panel of Fig. 3 shows the linear increment for different positions along the field line as the distribution of hot electrons changes adiabatically as per Eq. (7). One can see that along the field line in our simulation box, the growth rate does not become much smaller than the maximum growth rate at the equator.

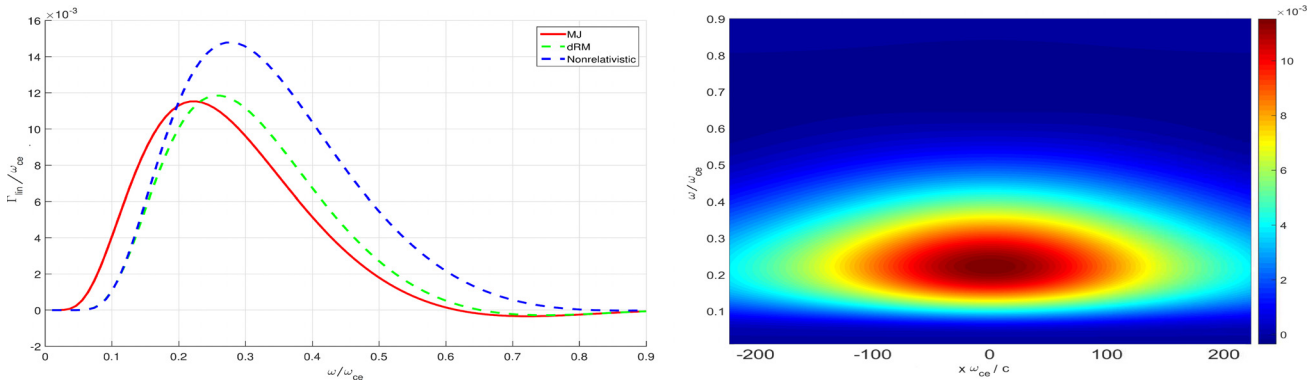

FIG. 3. (Left) Linear increment as a function of wave frequency. All the distributions have the following parameters: $p_{\|T} = 0.17mc$ ($T_{\|} \approx 15$ keV), $p_{\perp T} = 0.41mc$ ($T_{\perp} \approx 85$ keV), which correspond to temperature $T = 100$ (keV) and anisotropy angle $\delta = 0.4$ (rad). MJ stands for the anisotropic Maxwell–Jüttner distribution as per Eq. (3), dRM stands for direct extension of the biMaxwellian distribution to relativistic energies as per Eq. (4), and the "nonrelativistic" curve corresponds to the nonrelativistic form of expression for Γ_{lin}. (Right) Linear increment for the distribution (7) as a function of frequency and position along the field line with magnetic field inhomogeneity $\alpha = 0.5\times10^{-5}\,[\frac{\omega_{ce}^2}{c^2}]$.

IV. SIMULATION RESULTS

In this section, we present the results of chorus wave simulation with the TRISTAN-MP code for the parameters shown in Table I. Figure 4 demonstrates the case of a moderate inhomogeneity value, $\alpha = 0.5 \times 10^{-5}\,[\frac{\omega_{ce}^2}{c^2}]$. In the upper panel, the evolution of the transverse field $B_w(x,t) = \sqrt{B_y^2 + B_z^2}$ is shown. One can see that the waves are generated in a small region near the equator, despite the fact that the area with high Γ_{lin} is rather large (see Fig. 3), which is consistent with observations.[44] As the waves propagate away from the equator, they are amplified. White dashed lines mark the position, where the time variation of the wave-field is analyzed. The corresponding time dependencies of the B_y component are presented in the middle panels, and their wavelet spectrograms are shown in the bottom panels. To perform time-frequency

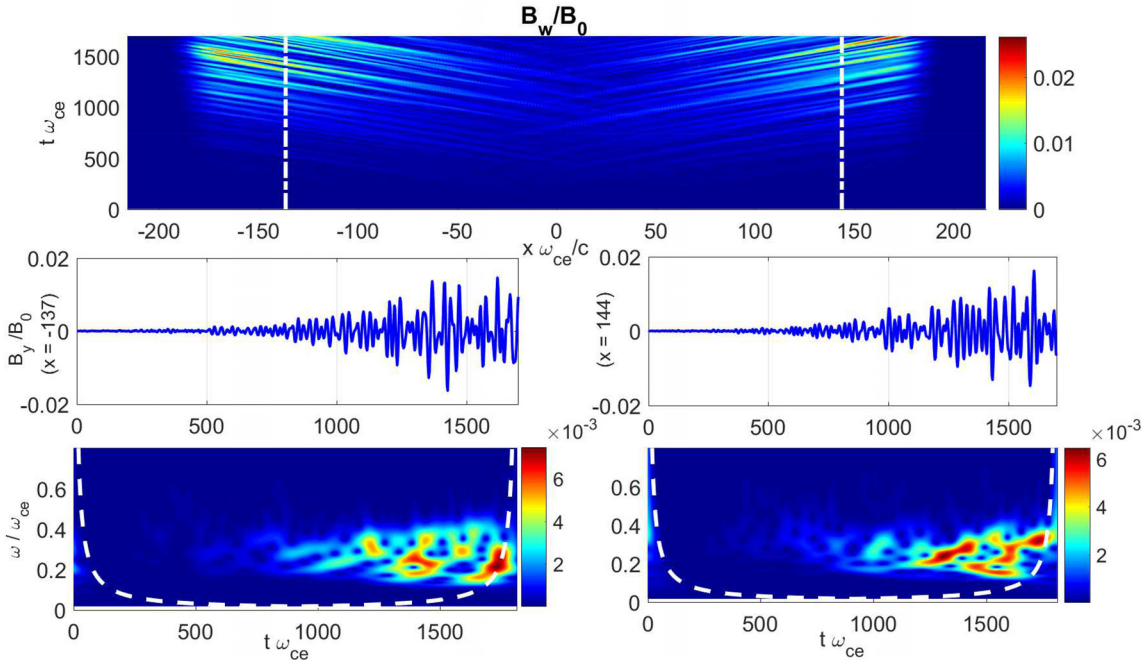

FIG. 4. Simulation results for an inhomogeneity parameter $\alpha = 0.5\times10^{-5}\,[\frac{\omega_{ce}^2}{c^2}]$. Upper panel presents the (x, t) distribution of the transverse field $B_w = \sqrt{B_y^2 + B_z^2}$, and white dashed lines indicate the positions along the field line where the field dependency on time is analyzed. These temporal forms are shown in the middle panels, and the bottom panels demonstrate their wavelet spectrograms. White lines in the spectrograms mark the cone of influence which indicates the area, where boundary effects might affect the spectrum. Chirping choruslike rising tone elements can be seen after the equator ($x = 144$ [c/ω_{ce}]).

analysis, we use the generalized Morse wavelets[45] with symmetry parameter $S = 3$ and time-bandwidth product $P^2 = 100$.

At the right position, two coherent rising-tone structures are formed with a chirping rate $\frac{\partial\omega}{\partial t} \approx 5\times10^{-4}\ [\frac{1}{\omega_{ce}^2}]$. This rate is consistent with other simulations.[31] Two elements overlap in time domain; hence, in order to analyze each element, we apply a mask to the spectrum to single out the corresponding elements. Figure 5 presents the results of singling out the first rising-tone element taken from the right column in Fig. 4. In Fig. 5, the B_y and B_z components of the wave field are shown in the panels with labels "1" and "2," respectively. Panels "a" ("1a" and "2a") show the total spectrogram for a given component of the wave field, while the corresponding temporal wave form is shown in panels "c" (time interval is limited to, approximately, element's duration). The singled-out rising-tone element is presented in panels "b" (B_y component of the element is shown in "1b" panel, and "2b" panel presents B_z component of the element), and panels "d" show element's temporal wave form, reconstructed via inverse wavelet transform. One can see that the amplitude's envelope of the rising tone element oscillates, revealing a subpacket structure of the element, consistent with observations.[1,46] B_y and B_z field components are shifted with respect to each other by a quarter of a wave period, as expected for right-hand polarized whistler-mode wave.

We performed three additional simulations, each with a different inhomogeneity parameter α to study its influence on wave generation. The results of all simulations are shown in Fig. 6 and are summarized in Table II. In Fig. 6, panels "a," we present the evolution of the transverse magnetic field in the whole simulation box along the field line. Panels "b" and "c" show the spectrograms of the B_y component at the given positions. The spectrogram of the selected singled-out element with its temporal behavior is shown in panels "d" and "e," respectively. We do not show here the B_z component of the field, only B_y, because the results are similar. For small inhomogeneity (left column of Fig. 6), chirping elements are rather short impulses with evidently large chirping rates. The longer wave packet, generated for $\alpha = 3.75\times10^{-6}\ [\frac{\omega_{ce}^2}{c^2}]$, has a well-formed subpacket structure with a lower chirping rate than the elements in the left column. Run 4 presented in the last column of Fig. 6 corresponds to the largest inhomogeneity and shows that no clear chirping structures are formed, in agreement with the theory of Omura *et al.*[11]

To calculate the frequency chirping rates, we fit the elements with curves $\omega_i(t)$ (shown in black in Fig. 6) and evaluate the corresponding derivatives $\partial\omega_i(t)/\partial t$. The chirping rate's numerical value, presented in Table II, is an average of $\partial\omega_i(t)/\partial t$ over ith element's duration. From Table II, one can see that as the inhomogeneity

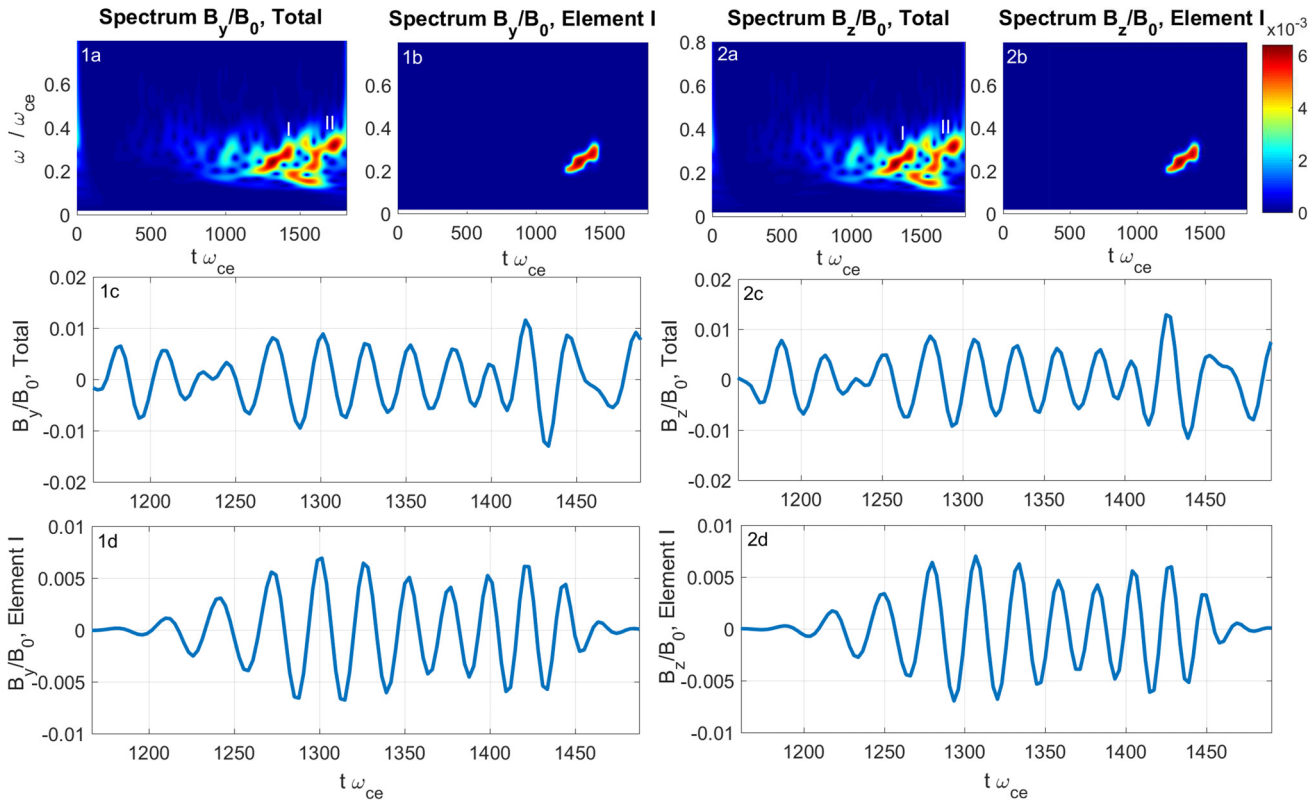

FIG. 5. Simulation results for an inhomogeneity parameter $\alpha = 0.5\times10^{-5}\ [\frac{\omega_{ce}^2}{c^2}]$. Panels, labeled "1" and "2," correspond to B_y and B_z components of the wave field. Full spectrograms for each component are indicated by label "a," and spectrograms with the given singled-out element are labeled by "b." Panels "c" present the temporal form of the total wave field in the time interval of the selected rising-tone element. Lower panels "d" show the temporal form of the selected rising-tone element, obtained by inverse wavelet transform from the spectrograms "b."

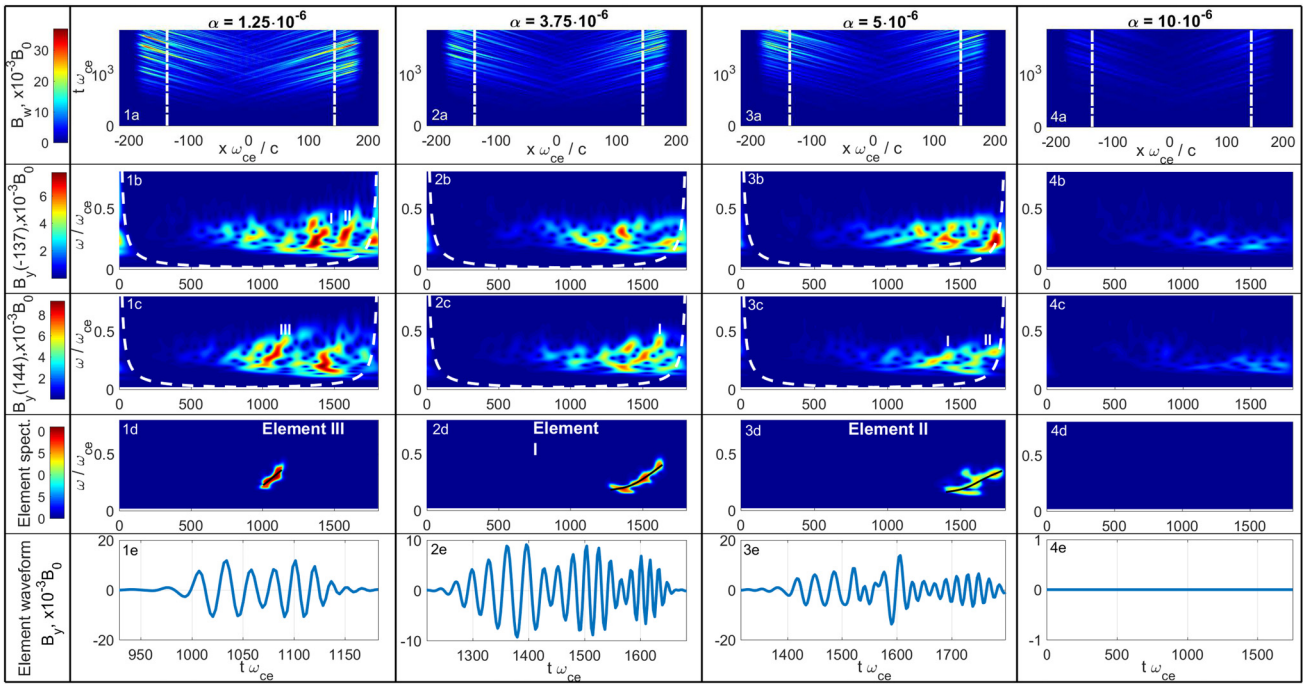

FIG. 6. Simulation results for different inhomogeneity parameters α, $[\omega_{ce}^2/c^2]$. Different runs are presented in different columns. Panels are labeled with numbers "1"–"4," enumerating the columns, and letters "a"–"d," indicating the rows. Panels "a" show transverse magnetic field $B_w = \sqrt{B_y^2 + B_z^2}$. Panels "b" and "c" show the spectrograms of $B_y(t)$ at given positions x ($x = -137$ and $x = 144$, respectively) along the field line. Roman numbers denote the rising-tone elements. White lines in the spectrograms mark the cone of influence which indicates the area, where the edge effects become important and affect the spectrum. Lower panels show the spectrogram of the selected rising-tone element (one for each run) and its temporal form. For the case $\alpha = 5 \times 10^{-6}[\omega_{ce}^2/c^2]$, we show the second element, as the first one is shown in Fig. 5. For the largest inhomogeneity, $\alpha = 10 \times 10^{-6}[\omega_{ce}^2/c^2]$, no clear chirping is observed.

parameter increases, the chirping rate decreases. We should note that a similar behavior was demonstrated in the recent PIC simulations with the dipole magnetic field.[47]

The theory[11] shows that the resonant wave-particle interaction resulting in the chorus wave generation is controlled by the following parameter, the total inhomogeneity ratio:

TABLE II. Simulation results for different inhomogeneity parameters α. The third column indicates the chirping rate obtained from the simulations. The fourth column shows the ratio of S_2 and S_1 from Eq. (17). The last column presents the theoretical estimates for the frequency chirping rate, Eq. (18). The averages are calculated over the duration of each element.

Run	α, $\left[\frac{\omega_{ce}^2}{c^2}\right]$	$\left\langle\frac{\partial\omega}{\partial t}\right\rangle$, $[\omega_{ce}^2]$ Simulation	$\frac{\langle S_2\rangle}{\langle S_1\rangle}$, %	$\left\langle\frac{\partial\omega}{\partial t}\right\rangle$, $[\omega_{ce}^2]$ Theory[11]
#1	1.25×10^{-6}	Element I: 0.9×10^{-3}	3%	0.8×10^{-3}
		Element II: 1.4×10^{-3}	2%	0.9×10^{-3}
		Element III: 1.0×10^{-3}	3%	1.2×10^{-3}
#2	3.75×10^{-6}	Element I: 0.6×10^{-3}	15%	0.6×10^{-3}
#3	5×10^{-6}	Element I: 0.4×10^{-3}	25%	0.5×10^{-3}
		Element II: 0.5×10^{-3}	22%	0.5×10^{-3}
#4	10×10^{-6}	No chirping elements		

$$S = -\frac{1}{\Omega_t^2 \xi^2}\left\{\gamma\left(1-\frac{v_r}{v_g}\right)^2\frac{\partial\omega}{\partial t} + \left[\frac{k\gamma v_\perp^2}{2\omega_{ce}} - \left(1+\frac{\xi^2}{2}\frac{\omega_{ce}-\gamma\omega}{\omega_{ce}-\omega}\right)v_r\right]\frac{\partial\omega_{ce}}{\partial x}\right\} \equiv -\frac{1}{\Omega_t^2\xi^2}(S_1+S_2). \tag{17}$$

Here, $\Omega_t = \sqrt{kv_\perp eB_w/m_e c}$ is the trapping frequency, v_r and v_g are the resonance and group velocities, and $\xi^2 = 1 - \omega^2/k^2c^2$. Theoretical estimations[11] demonstrate that the optimal value of the total inhomogeneity ratio is $S = -0.4$. It allows us to calculate the chirping rate at the equator, where $\partial\omega_{ce}/\partial x = 0$ (i.e., $S_2 = 0$ in Ref. 17). As the wave propagates away from the equator, the second term, which explicitly contains the spatial inhomogeneity, begins to contribute to S. Nevertheless, its contribution might be neglected at small distances from the equator. The fourth column of Table II contains the estimations of S_2 at the distances where the elements are analyzed. In these calculations, we took the average value at the equator for $v_\perp$. The estimates show that we can marginally neglect the S_2 term in Eq. (17). However, the chirping rate is different for the different inhomogeneity parameters α. This is due to the fact that the wave amplitudes are different in each simulation. We should emphasize that the spatial inhomogeneity manifests not only in the explicit term $\partial\omega_{ce}/\partial x$ of Eq. (17) but also in the adiabatic initial distribution, Eq. (7), where the density

and the effective temperature anisotropy of the hot electron population vary along the field line (see, e.g., Fig. 3).

Having said this, we estimate the theoretical chirping rates for each element as follows:

$$\frac{\partial\omega}{\partial t} = W[f(v_\perp)]K(\omega)\frac{B_w(t)}{B_0}, \tag{18}$$

that is, neglecting the second term in Eq. (17). The results are presented in the last column of Table II. Here, $K(\omega)$ depends on local wave frequency and $W[f(v_\perp)]$ depends on properties of the perpendicular velocity distribution function, f. Omura *et al.*[11] chose a simplified singular distribution function $f(v_\perp) \sim \delta(v_\perp - v_{\perp 0})$ and demonstrated that $K \sim v_{\perp 0}$ near the magnetic equator. However, this is not the case for our simulations, and it is difficult to generalize this formula for an arbitrary distribution function and to extrapolate it to the region away from the equator (see, e.g., Ref. 48 where an attempt to extend Omura *et al.* theory is proposed). Hence, to make an estimation, we assume that K depends on wave frequency as in Ref. 11, but for $W[f(v_\perp)]$ instead of $v_{\perp 0}$, we choose a constant value, such that the average theoretical and simulated chirping rates for Run 2 are equal. Comparison between numerical and theoretical rates shows a rather good agreement, except, perhaps, for the Element II in Run 1. The larger discrepancy in this case might be due to the fact that it is very short (in time) element, so an error in fitting could be large.

V. SUMMARY

In this paper, we have presented the results of numerical simulations of magnetospheric chorus wave generation with a 2D full particle-in-cell code called TRISTAN-MP. The waves are triggered by the whistler-mode instability of the anisotropic distribution function. While previous studies used extrapolation (4) of nonrelativistic biMaxwellian to the relativistic energies (with or without the loss-cone), we implemented the anisotropic version of the correct relativistic Maxwell–Jüttner distribution (1). The difference in the linear growth is perceptible (see Fig. 3) when compared to other distributions, despite the fact that the parallel energy is only slightly relativistic. This arises from the fact that perpendicular energy is relativistic, and the high-energy tail of the Maxwell–Jüttner distribution is essentially different from the simplified distribution (4).

We have successfully generated choruslike emissions. The results agree qualitatively with other numerical simulations.[12,31,49] Waves are generated near the equator, where the resonance condition is satisfied for a larger number of particles. Waves then propagate away from the equator, interacting with resonant particles and being amplified. For small background magnetic field inhomogeneities, coherent choruslike structures with chirping frequency are formed. To study each chirping element separately, we singled out the elements from the spectrograms, using a masking function. The excited rising-tone choruslike waves belong to the lower band ($\omega < 0.5\ \omega_{ce}$). Figures 5 and 6 (column 2) demonstrate the amplitude variation of the wave-packets, thus revealing the subpacket structure of the choruslike elements. For each chirping element, we calculated the chirping rate and demonstrated that this rate tends to decrease as the inhomogeneity of the background magnetic field increases. These results are summarized in Table II.

Theoretical estimations of the chirping rate made from Ref. 11 are in rather good agreement with our results. Our study shows that higher magnetic field inhomogeneity suppresses chorus wave generation. This is also consistent with Omura *et al.* theory,[15] which predicts the existence of threshold amplitude related to inhomogeneity, below which there is no non-linear interaction between particles and a wave. The threshold amplitude is related to the fact that particles cannot be trapped if the total inhomogeneity ratio $|S| \geq 1$. We should mention that both the frequency variation and the spatial inhomogeneity contribute to the total inhomogeneity ratio, Eq. (17).

In this paper, we specifically studied quasi-parallel wave generation. Thus, we were able to compare the results of our 2D simulations with previous 1D PIC simulations and theoretical predictions. Modeling magnetospheric chorus wave generation in a regime when the oblique waves are predominantly generated is an important and challenging problem, which is left for a future study.

ACKNOWLEDGMENTS

This work was supported by the National Science Foundation (NSF) Grant No. 1502923. We would like to acknowledge high-performance computing support from Cheyenne doi:10.5065/D6RX99HX provided by NCAR's Computational and Information Systems Laboratory, sponsored by NSF. The NJIT Kong cluster at New Jersey Institute of Technology (Newark, NJ, USA) was also used. I. Kuzichev would also like to acknowledge the support of the RBSPICE Instrument project by JHU/APL Subcontract No. 937836 to the New Jersey Institute of Technology under NASA Prime Contract No. NAS5-01072.

APPENDIX: TRISTAN-MP PIC CODE

The simulations were performed with the 2D TRISTAN-MP PIC code. This code is a development[37] of the TRISTAN code created by Buneman.[50] This massively parallelized (MP) code was successfully used to model relativistic[38] and nonrelativistic[39] shocks. The Maxwell's equations are solved in the code with the standard second-order Yee algorithm.[51] The TRISTAN-MP code provides the possibility to choose between the Vay scheme[52] and the Boris scheme[53] for the solver of the particle equations of motion. Vay[52] demonstrated that the Boris scheme might lead to appearance of a spurious force and suggested a scheme which would be free of this problem. This spurious force appears to be small enough for most cases, but there are known examples when it leads to significant errors.

One of the main changes introduced into the code is a numerical scheme that allows to inject two electron populations. This is crucial for simulation of the magnetospheric chorus waves generation. Also, particle sampling according to the anisotropic relativistic Maxwell distribution is implemented. This distribution is discussed in details in Sec. II. Reflecting boundary conditions were implemented in the code for the hot particles in order to simulate particle reflection due to the magnetic mirror force.

For the electromagnetic field, the code uses a cubic polynomial mask to damp the fields at the boundary. For the nonmodified finite-difference scheme, one has, for example, for the B_z and E_y components

$$B_z(x, y, t_{n+1}) = B_z(x, y, t_n) + C\left(\Delta_y E_x - \Delta_x E_y\right),$$
$$E_y(x, y, t_{n+1}) = E_y(x, y, t_n) + C\Delta_x B_z,$$

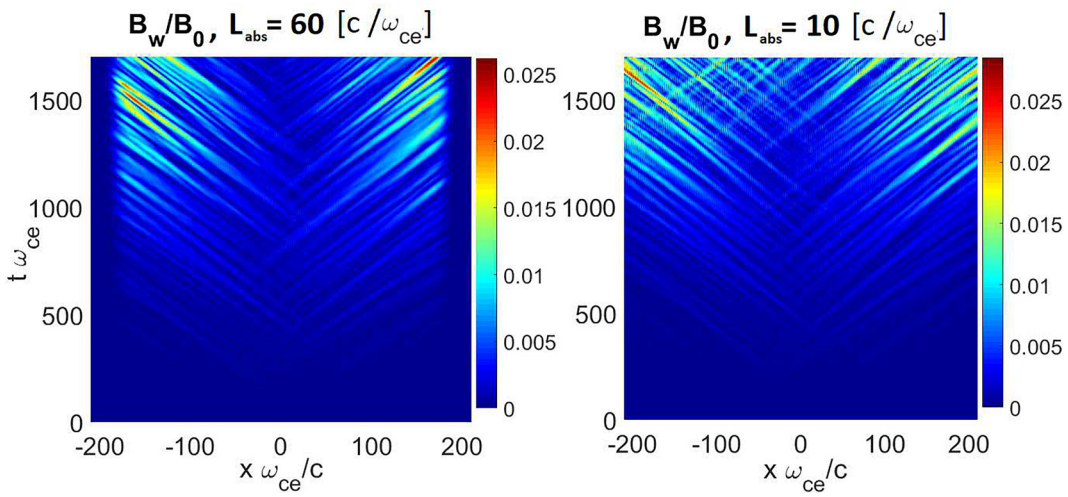

FIG. 7. Simulation results for the transverse field $B_w = \sqrt{B_y^2 + B_z^2}$ for a wide absorption boundary (left) and a narrow absorption boundary (right).

where C is a constant and Δ is the difference operator in the corresponding dimension. The masking changes these equations to the following ones:

$$B_z(x,y,t_{n+1}) = \left[B_z(x,y,t_n)(1+\lambda) + C\left(\Delta_y E_x - \Delta_x E_y\right)\right]/(1-\lambda),$$
$$E_y(x,y,t_{n+1}) = \left[E_y(x,y,t_n)(1+\lambda) + C\Delta_x B_z\right]/(1-\lambda),$$

with

$$\lambda = \begin{cases} 0, & \text{if } x \in \left[-\frac{L_x}{2} + L_{abs}, \frac{L_x}{2} - L_{abs}\right], \\ \frac{C}{6L_{abs}^3}\left(x + \frac{L_x}{2} - L_{abs}\right)^3, & \text{if } x < -\frac{L_x}{2} + L_{abs}, \\ \frac{C}{6L_{abs}^3}\left(\frac{L_x}{2} - x - L_{abs}\right)^3, & \text{if } x > \frac{L_x}{2} - L_{abs}. \end{cases}$$

Here, L_{abs} is the absorption length, i.e., the width of the absorption boundary. It is worth mentioning that this quantity cannot be taken as arbitrary small because it would lead to fast variation of the parameters of the Maxwell's equations and, consequently, lead to the strong reflection of the waves. Similar changes are introduced to other field equations. Figure 7 shows two simulations with different absorption lengths, with other parameters being fixed. The right panel demonstrates the case of very short absorption length, and strong reflection of the field from the boundary is observed. In the simulation with larger absorption length, shown in the left panel, there is no visible field reflection at the boundaries. It can be seen that, for the damping mask we use, it is possible to find an absorption length which would efficiently suppress the reflection, and simultaneously remaining small with respect to the total length of the system.

REFERENCES

[1]O. Santolik, D. A. Gurnett, J. S. Pickett, M. Parrot, and N. Cornilleau-Wehrlin, J. Geophys. Res.: Space Phys. **108**, 1278, https://doi.org/10.1029/2002JA009791 (2003).

[2]S. Kurita, H. Misawa, C. M. Cully, O. Le Contel, and V. Angelopoulos, Geophys. Res. Lett. **39**, L22102, https://doi.org/10.1029/2012GL053929 (2012).

[3]U. Taubenschuss, O. Santolík, D. B. Graham, H. Fu, Y. V. Khotyaintsev, and O. Le Contel, Geophys. Res. Lett. **42**, 8271, https://doi.org/10.1002/2015GL066004 (2015).

[4]W. Burtis and R. Helliwell, Planet. Space Sci. **24**, 1007 (1976).

[5]S. Kurita, Y. Katoh, Y. Omura, V. Angelopoulos, C. M. Cully, O. Le Contel, and H. Misawa, J. Geophys. Res.: Space Phys. **117**, A11223, https://doi.org/10.1029/2012JA018076 (2012).

[6]N. P. Meredith, R. B. Horne, and R. R. Anderson, J. Geophys. Res.: Space Phys. **106**, 13165, https://doi.org/10.1029/2000JA900156 (2001).

[7]R. M. Thorne, B. Ni, X. Tao, R. B. Horne, and N. P. Meredith, Nature **467**, 943 (2010).

[8]J. Bortnik and R. Thorne, J. Atmos. Sol. Terr. Phys. **69**, 378 (2007).

[9]T. F. Bell, J. Geophys. Res. **89**, 905, https://doi.org/10.1029/JA089iA02p00905 (1984).

[10]D. Shklyar and H. Matsumoto, Surv. Geophys. **30**, 55 (2009).

[11]Y. Omura, Y. Katoh, and D. Summers, J. Geophys. Res.: Space Phys. **113**, A04223, https://doi.org/10.1029/2007JA012622 (2008).

[12]M. Hikishima and Y. Omura, J. Geophys. Res.: Space Phys. **117**, A04226, https://doi.org/10.1029/2011JA017428 (2012).

[13]W. Li, J. Bortnik, R. M. Thorne, and V. Angelopoulos, J. Geophys. Res. **116**, A12205, https://doi.org/10.1029/2011ja017035 (2011).

[14]N. Haque, M. Spasojevic, O. Santolík, and U. S. Inan, J. Geophys. Res.: Space Phys. **115**, A00F07, https://doi.org/10.1029/2009JA014717 (2010).

[15]Y. Omura, M. Hikishima, Y. Katoh, D. Summers, and S. Yagitani, J. Geophys. Res. **114**, A07217, https://doi.org/10.1029/2009JA014206 (2009).

[16]Y. Omura, D. Nunn, and D. Summers, "Generation processes of whistler mode chorus emissions: Current status of nonlinear wave growth theory," in *Dynamics of the Earth's Radiation Belts and Inner Magnetosphere* (American Geophysical Union (AGU), 2013), pp. 243–254.

[17]A. R. Soto-Chavez, G. Wang, A. Bhattacharjee, G. Y. Fu, and H. M. Smith, Geophys. Res. Lett. **41**, 1838, https://doi.org/10.1002/2014GL059320 (2014).

[18]H. Huang, Z. B. Wang, X. Tao, and X. G. Wang, Phys. Plasmas **24**, 102901 (2017).

[19]P. Hosseini, M. Gołkowski, and V. Harid, Geophys. Res. Lett. **46**, 37, https://doi.org/10.1029/2018GL081391 (2019).

[20]V. Y. Trakhtengerts, J. Geophys. Res. **100**, 17205, https://doi.org/10.1029/95JA00843 (1995).

[21]E. Titova, A. Demekhov, B. Kozelov, O. Santolík, E. Macúšová, J.-L. Rauch, J.-G. Trotignon, D. Gurnett, and J. Pickett, J. Geophys. Res.: Space Phys. **117**, A08210, https://doi.org/10.1029/2012JA017713 (2012).

[22]D. Nunn and Y. Omura, J. Geophys. Res.: Space Phys. **117**, A08228, https://doi.org/10.1029/2012JA017557 (2012).
[23]A. G. Demekhov, Radiophys. Quantum Electron. **53**, 609 (2011).
[24]F. Filbet, E. Sonnendrücker, and P. Bertrand, J. Comput. Phys. **172**, 166 (2001).
[25]D. Nunn, J. Comput. Phys. **108**, 180 (1993).
[26]D. Nunn, O. Santolik, M. Rycroft, and V. Trakhtengerts, Ann. Geophys. **27**, 2341 (2009).
[27]V. Harid, M. Gołkowski, T. Bell, J. D. Li, and U. S. Inan, Geophys. Res. Lett. **41**, 8193, https://doi.org/10.1002/2014GL061787 (2014).
[28]C. K. Birdsall and A. B. Langdon, *Plasma Physics via Computer Simulation*, Series in Plasma Physics (CRC Press, 2004).
[29]Y. Katoh and Y. Omura, J. Geophys. Res.: Space Phys. **111**, A12207, https://doi.org/10.1029/2006JA011704 (2006).
[30]Y. Katoh and Y. Omura, J. Geophys. Res.: Space Phys. **116**, A07201, https://doi.org/10.1029/2011JA016496 (2011).
[31]M. Hikishima, S. Yagitani, Y. Omura, and I. Nagano, J. Geophys. Res.: Space Phys. **114**, a01203, https://doi.org/10.1029/2008JA013625 (2009).
[32]X. Tao, J. Geophys. Res.: Space Phys. **119**, 3362, https://doi.org/10.1002/2014JA019820 (2014).
[33]C. Yue, X. An, J. Bortnik, Q. Ma, W. Li, R. M. Thorne, G. D. Reeves, M. Gkioulidou, D. G. Mitchell, and C. A. Kletzing, Geophys. Res. Lett. **43**, 7804, https://doi.org/10.1002/2016GL070084 (2016).
[34]E. E. Titova, B. V. Kozelov, F. Jiricek, J. Smilauer, A. G. Demekhov, and V. Y. Trakhtengerts, Ann. Geophys. **21**, 1073 (2003).
[35]E. Macúšová, O. Santolík, P. Décréau, A. G. Demekhov, D. Nunn, D. A. Gurnett, J. S. Pickett, E. E. Titova, B. V. Kozelov, J.-L. Rauch, and J.-G. Trotignon, J. Geophys. Res.: Space Phys. **115**, A12257, https://doi.org/10.1029/2010JA015468 (2010).
[36]M. Gołkowski, V. Harid, and P. Hosseini, Front. Astron. Space Sci. **6**, 2 (2019).
[37]A. Spitkovsky, AIP Conf. Proc. **801**, 345 (2005).
[38]A. Spitkovsky, Astrophys. J. Lett. **682**, L5 (2008).
[39]J. Park, D. Caprioli, and A. Spitkovsky, Phys. Rev. Lett. **114**, 085003 (2015).
[40]G. Livadiotis, Ann. Geophys. **34**, 1145 (2016).
[41]Y. Katoh, Y. Omura, Y. Miyake, H. Usui, and H. Nakashima, J. Geophys. Res.: Space Phys. **123**, 1165, https://doi.org/10.1002/2017JA024801 (2018).
[42]C. F. Kennel and H. E. Petschek, J. Geophys. Res. **71**, 1, https://doi.org/10.1029/JZ071i001p00001 (1966).
[43]F. Xiao, R. M. Thorne, and D. Summers, Phys. Plasmas **5**, 2489 (1998).
[44]M. J. LeDocq, D. A. Gurnett, and G. B. Hospodarsky, Geophys. Res. Lett. **25**, 4063, https://doi.org/10.1029/1998GL900071 (1998).
[45]S. C. Olhede and A. T. Walden, IEEE Trans. Signal Process. **50**, 2661 (2002).
[46]O. Santolík, C. A. Kletzing, W. S. Kurth, G. B. Hospodarsky, and S. R. Bounds, Geophys. Res. Lett. **41**, 293, https://doi.org/10.1002/2013GL058889 (2014).
[47]Q. Lu, Y. Ke, X. Wang, K. Liu, X. Gao, L. Chen, and S. Wang, J. Geophys. Res.: Space Phys. **124**, 1, https://doi.org/10.1029/2019ja026586 (2019).
[48]M. Gołkowski and A. R. Gibby, Phys. Plasmas **24**, 092904 (2017).
[49]Y. Katoh and Y. Omura, J. Geophys. Res.: Space Phys. **118**, 4189, https://doi.org/10.1002/jgra.50395 (2013).
[50]O. Buneman, *TRISTAN: The 3-D Electromagnetic Particle PIC Code* (Terra Scientific, Tokyo, 1993), Chap. 3, pp. 67–84.
[51]K. Yee, IEEE Trans. Antennas Propag. **14**, 302 (1966).
[52]J.-L. Vay, Phys. Plasmas **15**, 056701 (2008).
[53]J. P. Boris, in *Proceedings of the Fourth Conference on Numerical Simulation Plasmas* (Naval Research Laboratory, Washington, D.C., 1970), pp. 3–67.